Article

NiO/MnFe$_2$O$_4$ Nanocomposite Photoluminescence, Structural, Morphological, Magnetic, and Optical Properties: Photocatalytic Removal of Cresol Red under Visible Light Irradiation

Muhammad Amjad, Ismat Bibi,* Farzana Majid, Kashif Jilani, Misbah Sultan, Qasim Raza,
Aamir Ghafoor, Norah Alwadai,* Arif Nazir, and Munawar Iqbal*

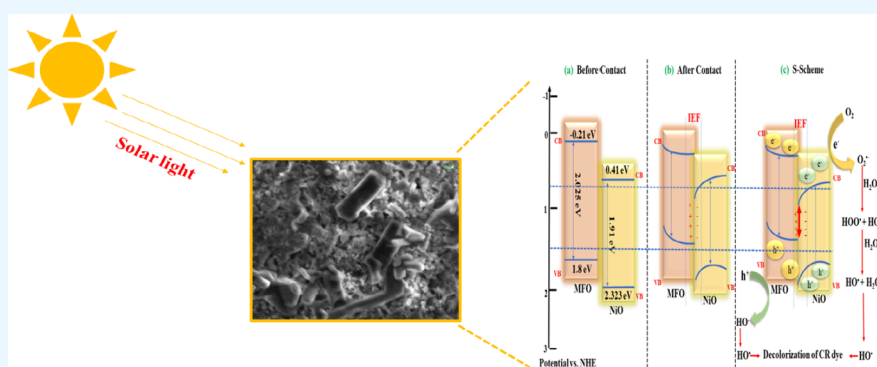Cite This: *ACS Omega* 2024, 9, 20876−20890

Read Online

ACCESS | Metrics & More | Article Recommendations | SI Supporting Information

ABSTRACT: In this study, pure nickel oxide (NiO), manganese ferrite (MnFe$_2$O$_4$ or MFO), and binary nickel oxide/manganese ferrite (NiO/MFO1−4) nanocomposites (NCs) were synthesized using the Sol−Gel method. A comprehensive investigation into their photoluminescence, structural, morphological, magnetic, optical, and photocatalytic properties was conducted. Raman analysis, UV−Vis spectroscopy, Fourier-transform infrared spectroscopy, scanning electron microscopy, and X-ray diffraction techniques were used to characterize the materials. The synthesized samples exhibited superparamagnetic behavior, as revealed by our analysis of their magnetic properties. A lower recombination rate was shown by the photoluminescence analysis, which is helpful for raising photocatalytic activity. The photocatalytic activity was evaluated for the degradation of Cresol Red (CR) dye. 91.6% of CR dye was degraded by NiO/MFO-4 nanocomposite, and the NC dosage as well as solution pH affected the photocatalytic performance significantly. In four sequential photocatalytic cycles, the magnetically separable NCs were stable and recyclable. The enhanced photocatalytic activity and magnetic separability revealed the potential application of NiO/MFO-4 as an efficient photocatalyst for the removal of dyes from industrial wastewater under solar light irradiation.

1. INTRODUCTION

Water contamination caused by dyes, even when present in low concentrations, poses a significant threat to aquatic ecosystems and human well-being. This issue is prevalent across various industries, such as textiles, food production, leather, plastics, paper, pharmaceuticals, and cosmetics, where dyes are extensively utilized. Among these, the textile sector stands out as the largest consumer of dyes, and due to its substantial water consumption, approximately 90% of the water employed in dyeing processes eventually becomes wastewater. A substantial proportion of textile dyes exhibit nonbiodegradable properties, and in some cases, they have been linked to potential carcinogenic effects. Consequently, it is imperative that, before discharging these charged effluents into natural water bodies, effective treatment measures are implemented to purify the wastewater.[1,2]

The traditional methods for treating textile wastewater have been applied, such as physical and biological methods. These techniques are costly and ineffective at low concentrations; nevertheless, they simply move the pollutants from the aqueous to the solid phase.[3−7] For these reasons, the community of researchers continues to be interested in finding low-cost methods for the treatment of wastewater.[8,9] In this regard, advanced oxidation methods for eliminating resistant or refractory pollutants are highly effective, which include redox

reactions, photocatalytic degradation, ozonation, and hydrogen peroxide oxidation-based advanced oxidation processes.[10,11]

One promising way to address the serious issue of water contamination is through the use of photocatalysis. Using photocatalysts, which are semiconductors that react with visible or UV light, this simple process does not require complicated equipment. As the boundary between the valence band (VB) and the conduction band (CB) in the semiconductor structure, the band gap energy (E_g) is crucial to this process.[10] The performance of the photocatalytic reaction depends on the gap and energetic location of CB and VB. NiO is widely employed in photocatalytic applications in the sectors of energy and the environment. It has intriguing photocatalytic effectiveness, because it is biocompatible, chemically stable, exhibits excellent photosensitivity, is inexpensive, has high redox potential, is nontoxic, and is environmentally friendly.[12] The extended band gap energy of 3.6 eV limits its responsiveness to UV radiation, which makes up a minimal portion of the solar light energy reaching our planet. Although UV light can be artificially generated, it poses significant risks to human health and necessitates meticulous handling. Notably, the photoexcited electron−hole (e^-h^+) pairs rapidly recombine on the surface. Furthermore, it is imperative to extract the catalysts from the liquid post-treatment for potential reuse, a process that incurs substantial costs and time expenditures.[10,11]

Addressing the separation challenge can be achieved by anchoring metal oxides onto solid substrates such as glass, ceramics, polymers, zeolites, or sand. However, this approach comes with certain drawbacks, including a reduction in surface area, limited interaction with the reaction medium, and constraints on the photocatalyst's exposure to light. Consequently, there has been a significant surge of interest in leveraging magnetic nanoparticles to bolster, encapsulate, or synergize with NiO, aiming to amplify the photocatalytic performance.[13] Magnetic nanoparticles serve a dual purpose: first, they enhance the photocatalytic capability of materials like NiO, enabling more efficient light absorption within the visible spectrum. Second, they facilitate the convenient removal of solid residues from treated water by applying an external magnetic field.[10,11] High mechanical toughness, a low band gap that is suitable for photocatalytic degradation under visible light, chemical inertness, excellent photonic absorption, easy recovery from reaction mixtures due to high magnetic property, relatively low Curie temperature (580 K), a high surface area to volume ratio, a mild saturation magnetization, and straightforward fabrication methods are all characteristics of $MnFe_2O_4$ magnetic nanoparticles. Due to weaker photoelectric conversion characteristics and lower VB edge potentials, it is not photocatalytically active.[14] These problems may be resolved by mixing ferrite with another semiconductor, which will enhance the charge separation effect. Therefore, $MnFe_2O_4$ should be coupled with a wide band gap semiconductor to increase its photocatalytic activity (PCA) under visible light. It is mainly believed that the unique semiconductor properties of $MnFe_2O_4$ and NiO—$MnFe_2O_4$ being an n-type semiconductor and NiO being a p-type semiconductor—are responsible for the increased PCA. The creation of a p-n heterojunction facilitates this. Electrons can move from the Fermi level of NiO to that of $MnFe_2O_4$ as a result of this heterojunction, continuing until their Fermi levels reach equilibrium. As a result, this process produces negative charges across $MnFe_2O_4$ and positive charges within the junction area of NiO.[11,15]

In photocatalytic applications, the capacity for the reuse of photocatalysts following treatment is a critical and cost-effective factor. But their separation for reuse is challenging, takes a lot of time, and expensive, particularly on a commercial scale. Using a catalyst that is recyclable and repeatable, magnetic nanoparticles are sufficient to address this problem.[10,11,16] Combining metal oxides such as NiO with spinel ferrites such as $MnFe_2O_4$ is a potentially effective way to boost PCA for the removal of organic contaminants. Spinel ferrites can be added to materials to increase their structural stability, promote photosensitization, decrease the bandgap, and increase the number of active adsorption sites.[17] In this regard, the combination of metal oxides (NiO) and spinel magnetic nanoparticles ($MnFe_2O_4$) as a composite system for the photodegradation of organic contaminants deserves much attention.[18,19]

Based on the aforementioned facts, NiO, MFO, and NiO/MFO(1−4) photocatalysts were fabricated by sol−gel route. A model chemical, the cationic dye Cresol Red($C_{21}H_{18}O_5S$, CR), was used to investigate the PCA under visible light. Additionally, the photoluminescence (PL), structural, morphological, magnetic, and optical properties of NiO/MFO(1−4) nanocomposite were also investigated.

2. MATERIALS AND METHODS

2.1. Chemicals and Reagents. Manganese nitrate Mn-$(NO_3)_2\cdot4H_2O$, iron nitrate $Fe(NO_3)_3\cdot9H_2O$, citric acid $C_6H_8O_7$, ammonia NH_3, distilled water, and CR ($C_{21}H_{18}O_5S$) were the materials used in this investigation. These chemicals were procured from Sigma-Aldrich. Without any additional processing, all of the chemicals used in this investigation were analytical grade when they were purchased and utilized.

2.2. Synthesis of MFO NPs. Manganese ferrites ($MnFe_2O_4$) nanoparticles were prepared by sol−gel autocombustion method. To prepare a mixed solution, a stoichiometric amount of manganese nitrate ($Mn(NO_3)_2\cdot4H_2O$), iron nitrate ($Fe(NO_3)_3\cdot9H_2O$), and citric acid ($C_6H_8O_7$) was dissolved in water with constant stirring. With the addition of ammonia, the pH of the solution was raised to 10. The reaction process was performed in an air-filled environment. For homogeneity, the solution was continually stirred. After 4 h of stirring, the mixture was heated to 80 °C and stirred until it solidified into a homogeneous viscous gel. The viscous gel underwent autocombustion, resulting in loose, flaky, and darkened powder, which was dried at 180 °C in the oven before being calcined for 2 h at 600 °C in the furnace. The obtained brown manganese ferrites were ground to a fine powder.

2.3. Synthesis of NiO NPs. The synthesis of NiO nanoparticles involved the sol−gel autocombustion method. After nickel nitrate was dissolved in distilled water, citric acid was continuously added as a surfactant. The solutions were mixed using a magnetic stirrer for 4 h until complete chemical dissolution. After that, ammonia was added little by little until the pH reached 10, at which point a light greenish sol was formed. At 80 °C, the liquids were steadily heated until a thick green gel was formed. The gel product is then dried at 80 °C and calcined at 450 °C for 2 h. A fine black powder is obtained.

2.4. Synthesis of NiO/MFO(1−4) NCs. Following the synthesis of the aforementioned nanomaterials, the ultrasonication process was used to synthesize various composi-
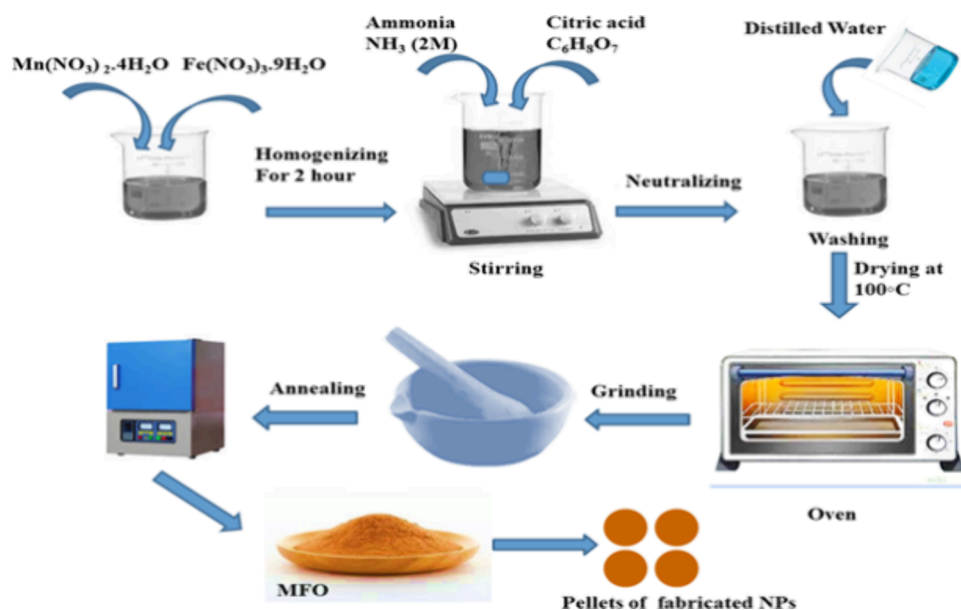
Figure 1. The schematic diagram for the synthesis of MFO nanomaterials (photograph courtesy of Muhammad Amjad. Copyright 2023).

tions. To achieve homogeneous mixing of both nanomaterials, various concentrations of nickel oxide and manganese ferrites were introduced to water with 1 h of stirring. Later, the synthesized material was dried in an oven at 90 °C. The dry material was thoroughly ground in a pestle and mortar to produce nanocomposites, each of which included varying amounts of nickel oxide and manganese ferrites (Figure 1). To obtain a series of samples, different percentages of MFO were used. The obtained samples were designated as 1% NiO/MFO-1, 5% NiO/MFO-2, 10% NiO/MFO-3, and 20% NiO/MFO-4.

2.5. Characterization. Various techniques were employed to characterize the synthesized pure NiO, MFO, and NiO/MFO(1−4) nanocomposites (NCs). The structural properties of all samples were examined through X-ray diffraction (XRD) analysis utilizing a Philips-x pert PRO 3040/60 X-ray diffractometer with Cu−K radiation (wavelength of 1.54 nm). The morphology of the nanocomposites was investigated using scanning electron microscopy (SEM) with a JEOL JSM-6360LA instrument. Surface functional groups were probed by using a PerkinElmer FT-IR spectrometer. The diffuse reflectance spectrum (DRS) in the UV−visible region was measured using a Cary 100 UV−visible spectrophotometer. PL parameters were recorded at room temperature using a Varian Cary eclipse fluorescence spectrophotometer. Magnetic properties were determined through magnetization measurements conducted with a vibrating sample magnetometer (VSM-LakeShore 7304 model).

2.6. PCA. By degrading CR dye under visible light irradiation, the PCA of the synthesized NiO, MFO, and NiO/MFO(1−4) nanocomposites (NCs) was evaluated. To achieve adsorption/desorption equilibrium, 10 mg of the catalyst was dissolved in 50 mL of CR dye solution (10 mg/L) in the experimental setup. The resulting suspension was then continuously stirred for 30 min in the dark. After that, the prepared mixtures were exposed to 200 W of visible light for 80 min. About 2 mL of aliquot was withdrawn from the reacting mixture after every 10 min interval, centrifuged, and analyzed to calculate the residual concentration of CR by

measuring its absorbance. Equation 1 was used to calculate the percentage degradation of CR dye.

$$Degradation\% = \frac{(A' - A)}{A'} \times 100\% \tag{1}$$

where, A' and A are the absorbance values of at tome zero and t, respectively.

3. RESULTS AND DISCUSSION

3.1. Powder XRD Analysis. Figure 2 shows the diffraction peaks of pure MFO, NiO, and NiO/MFO(1−4) NCs. In the
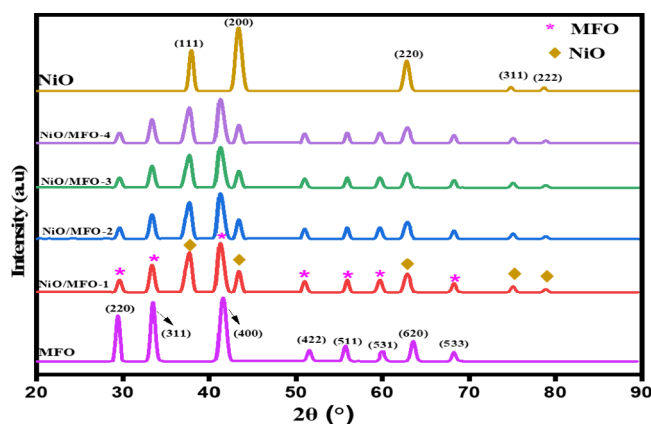

Figure 2. XRD patterns of pure NiO, MFO, and NiO/MFO(1−4) nanocomposites.

case of NiO, the diffraction peaks appeared at 2-theta of 37.5°, 43.4°, 62.8°, 74.8°, and 78.6° were indexed to (111), (200), (220), (311), and (222) planes, respectively and were well matched with JCPDS card No. (00-001-1239) of cubic NiO with space group fm3m.[20] While for MFO, the crystalline peaks evolved at 2-theta of 29.5°, 33.9°, 42.3°, 51.8°, 55.7°, 59.9°, 63.5°, and 68.5° were attributed to (220), (311), (400), (422), (511), (531), (620), and (533) planes, respectively, which are in agreement with JCPDS 00-002-1392.[21] In the case of NiO/MFO(1−4) NCs, the characteristic diffraction

Table 1. Structural Parameters of NiO, MFO, and Nanocomposite NiO/MFO(1−4)

samples	NiO	MFO	NiO/MFO1	NiO/MFO2	NiO/MFO3	NiO/MFO4
crystallite size (nm)	22.7	21.5	28.3	32.7	34.6	38.9
strain ($\delta \times 10^{-3}$ (nm^{-2}))	11.95	9.17	8.12	7.97	7.82	7.64
dislocation density ($\varepsilon \times 10^{-3}$)	6.12	5.62	6.10	6.04	5.96	5.79
X-ray density (g cm^{-3})	4.87	5.13	5.02	4.84	4.70	4.56
bulk density (g cm^{-3})	1.95	2.02	1.62	1.40	1.24	1.02
porosity (%)	60	62	67	71	74	78
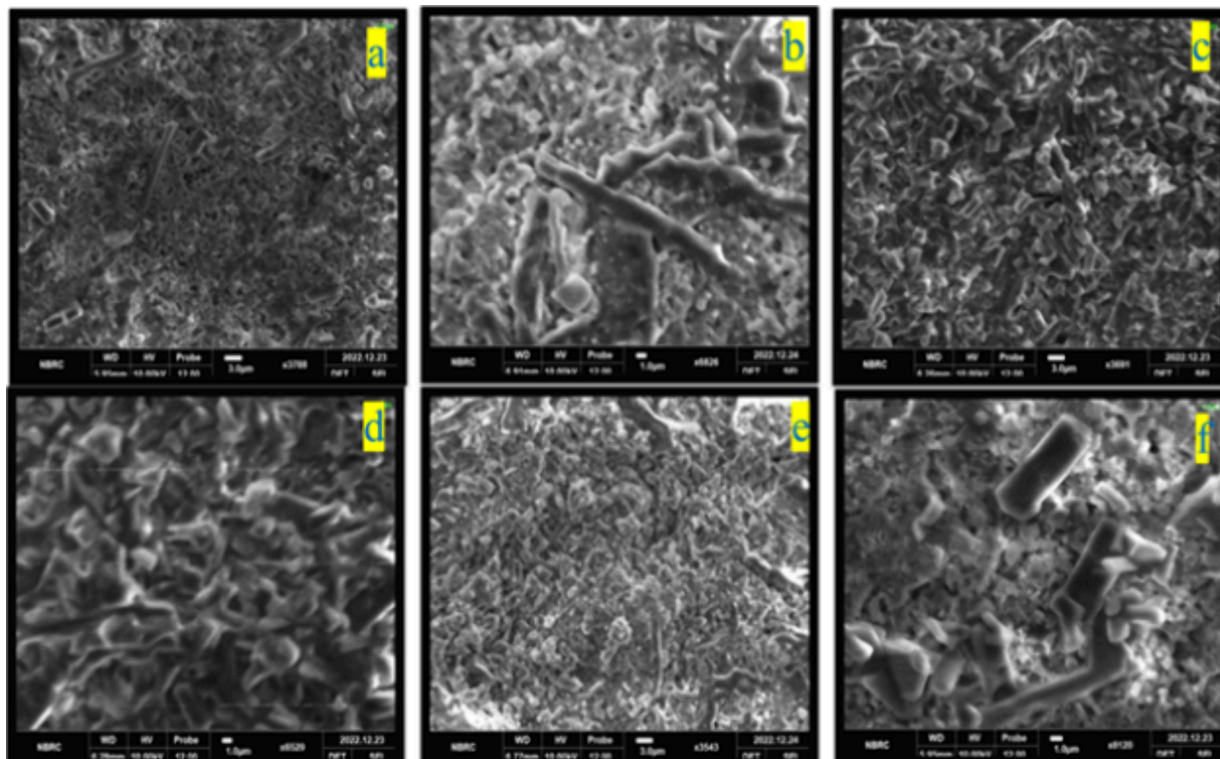
Figure 3. (a, b) SEM morphology of NiO, MFO and (c−f) NiO/MFO(1−4) NCs.

peaks of MFO and NiO were observed without the appearance of any secondary peak, which indicated the pure phase formation of the composite. The crystallite size of synthesized nanomaterials was estimated by the Scherer formula,[22] as shown in eq 2, where k is the Scherrer constant (~0.99), λ is the X-ray wavelength, β is the fwhm, and θ represents Bragg's angle. The estimated average crystallite sizes for NiO and MFO were found to be 21.5 and 22.7 nm, respectively. While the average crystallite size of the NCs NiO/MFO(1−4) was 28.3 32.7, 34.6, and 38.9 nm, respectively.

$$D = \frac{k\lambda}{\beta \cos \theta} \quad (2)$$

Table 1 shows the behavior of XRD, where there is an increase in crystallite size and a decrease in microstrain (ε) and dislocation density (δ). As the crystallite size increases, the peaks become sharper and narrower. This is because larger crystallites diffract X-rays more efficiently, leading to better-defined diffraction peaks.[23] These distortions may be caused by several reasons, including lattice defects, grain boundaries, or material stresses. As the microstrain decreases, the diffraction peaks become narrower, and the broadening effect is reduced.[24] Moreover, the decrease in the dislocation density

as given in Table 1 infers that the lattice becomes more ordered, and the distortions from the dislocation are reduced. As a result, the diffraction peaks become sharper and narrower.[25] The porosity (%) was calculated for pure NiO, MFO was 60 and 62%, while NCs NiO/MFO(1−4) have 67, 71, 74, and 78%, respectively. The enhanced % porosity of NCs indicates better adsorption behavior which results in efficient photocatalytic degradation of CR dye.[26] Moreover, the X-ray density was calculated to be higher than the bulk density due to the existence of pores. Formation of highly porous NCs NiO/MFO(1−4) is ideal for photocatalytic processes.[27]

Critical structural factors, such as dislocation density and microstrain were quantified using the equations.[28,29]

$$\delta = 1/D^2 \quad (3)$$

$$\varepsilon = \frac{\beta}{4 \tan \theta} \quad (4)$$

3.2. Surface Morphology. SEM was used to describe the material's morphology (SEM JEOL JSM-6360LA). Figure 3 depicts the surface morphology of pure NiO, MFO (a, b), and NiO/MFO(1−4) (c−f), respectively. The SEM of the NiO at 20,000 magnifications reveals that the sample contains irregularly shaped particles. The bigger particles are not

spherical. MFO has an evenly distributed, homogeneous grain shape with an average particle diameter of 22.7 nm. Because of the magnetic properties of MFO NPs, the NiO/MFO-1 particle shape is nonhomogeneous, and agglomeration is evident.[30] Meanwhile, the NiO/MFO(2−4) morphology is a homogeneous rectangular plate with an average particle diameter of less than 100 nm.

3.3. FT-IR Analysis. Fourier transform infrared spectroscopy (FT-IR) is used to study the functional groups of nanomaterials.[31] The FT-IR spectra of pure NiO, MFO, and NiO/MFO(1−4) are depicted in Figure 4. NiO nanoparticles
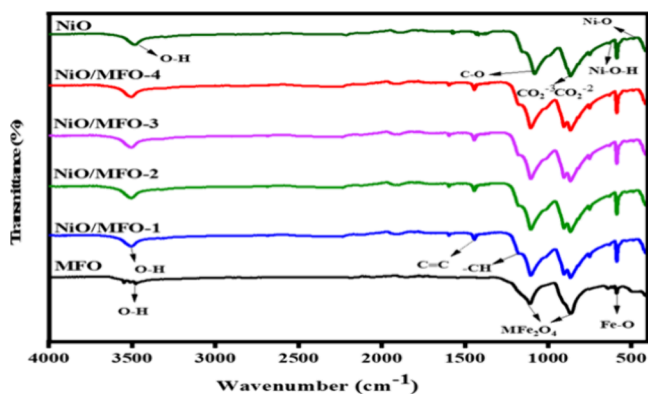

Figure 4. FT-IR analysis of pure NiO and MFO and NiO/MFO(1−4) NC material.

demonstrate that the peak at 475 cm^{-1} corresponds to the stretching mode of Ni−O nanoparticles.[32] The absorption band at 629 cm^{-1} is attributed to the Ni−O−H stretching bond.[33] CO_2^{-3} CO_2^{-2} ions are responsible for the broad absorption band of about 860 cm^{-1} and stretching is responsible for the peak at 1090 cm^{-1} intercalated. C−O species' stretching and bending vibrations. The O−H stretching modes of water are attributed to the large absorption band at 3460 cm^{-1}. Similarly, MFO contains ferrites, as demonstrated by the high absorption peaks that appear below 1000 cm^{-1}.[34,35] Stretching at 580 cm^{-1} is caused by the vibrations of Fe−O, which are signs that a spinel ferrite structure is formed. In ferrites, the metal ions are located in two distinct lattice interstices. One is positioned at the tetrahedral site and the other is located at the octahedral site.[36] According to FT-IR spectra, the octahedral site is correlated with the low-frequency band at 1090 cm^{-1} and the tetrahedral site is correlated with the high-frequency band at 875 cm^{-1}. The high degree of crystallinity of MFO NPs is coupled with these bands' sharpness. The O−H stretching vibration of the adsorbed water molecules is coupled with a large vibration band at 3452 cm^{-1}, which indicates a greater surface OH. The coupled peaks of NiO and MFO were detected in NC samples of NiO/MFO(1−4). According to NCs, the low-intensity peaks shown at 1122 and 1353 cm^{-1} can be attributed to −CH and C=C, respectively.[37]

3.4. Raman Analysis. Raman spectroscopy of pure NiO, MFO, and NiO/MFO(1−4) NC materials was performed, which shows the molecular vibrations through which interaction and chemical surroundings.[38] Raman spectra of NiO, MFO, and NiO/MFO(1−4) NC materials across the wavenumber region of 140 to 1800 cm^{-1} at 298 K. Figure 5 shows the Raman spectrum of the NiO nanoparticles. The five bands correspond to one-phonon LO modes (at ∼480 cm^{-1}),

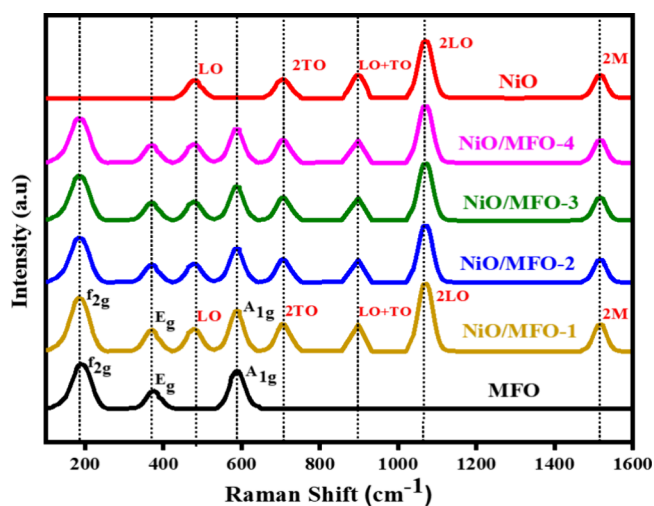**Figure 5.** Raman spectra of pure NiO, MFO, and NiO/MFO(1−4) NCs.

two-phonon 2TO modes (at ∼707 cm^{-1}), TO + LO (at ∼902 cm^{-1}), 2LO (at ∼1074 cm^{-1}), and 2 M (at ∼1518 cm^{-1}) modes, respectively.[39] In the Raman spectrum of MnFe$_2$O$_4$ nanoparticles (Figure 5), the F_{2g} band (at ∼ 190 cm^{-1}) is due to the translational movement of the whole tetrahedron (FeO$_4$), the E_g band (at ∼375 cm^{-1}) is due to the asymmetric and symmetric bending of O concerning Fe, and the A_{1g} band (at ∼590 cm^{-1}) is due to the symmetric stretching of oxygen atoms along Fe−O (or Mn−O) tetrahedral bonds.[40] The asymmetric stretching of the Fe/Mn−O bonds results in the E_g band, which is one of the peaks in the Raman spectrum of the NiO/MFO(1−4) nanocomposites (NCs) that are attributed to MFO. Furthermore, the presence of NiO and MFO in the NCs is confirmed by the E_{2g} band characteristic of NiO nanoparticles. The Raman spectrum observations show that the band locations shift toward shorter wavenumbers as the MFO content increases. Moreover, the presence of ion replacements and vacancies, as indicated by a decrease in Raman peak intensities, suggests the successful formation of the nanocomposites.[41]

3.5. PL Analysis. The PL spectrum of NiO, MFO, and NCs NiO/MFO(1−4) is shown in Figure 6. PL analysis was used to investigate the charge separation abilities and
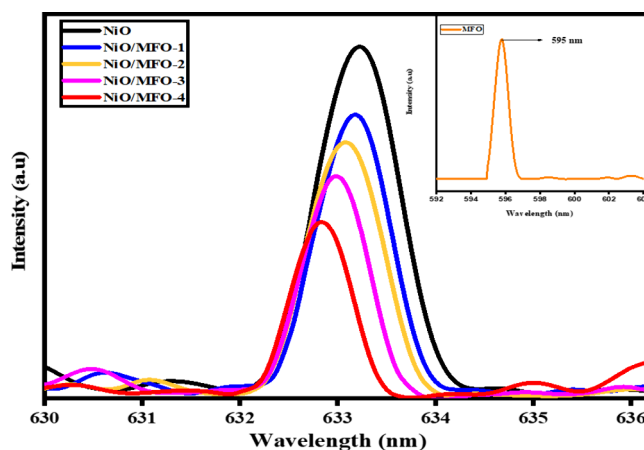

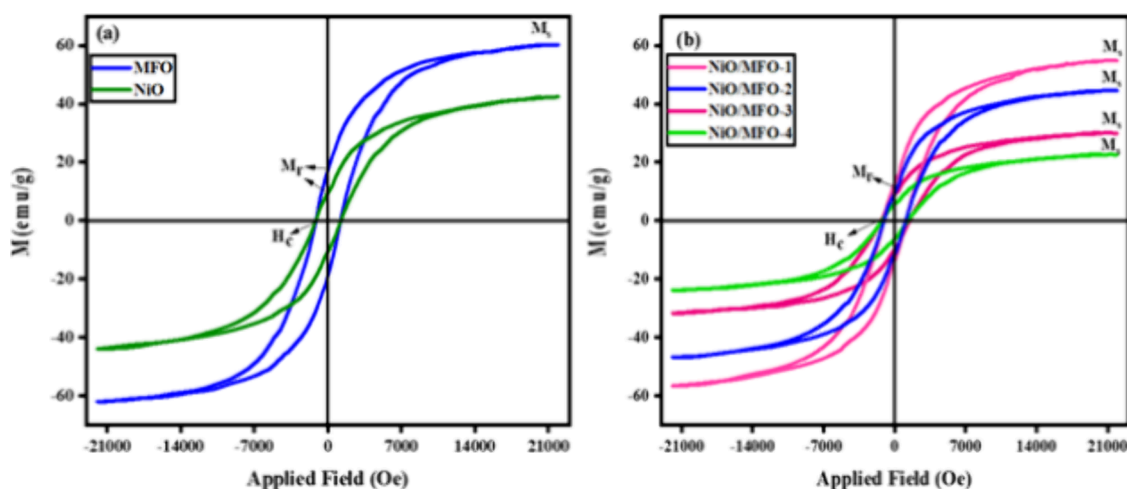**Figure 6.** Photoluminescence spectra of NiO, MFO, and NiO/MFO(1−4)NCs.

Figure 7. (a) Magnetic hysteresis loops of NiO and MFO and (b) hysteresis loops of NiO/MFO(1−4) NCs.

recombination of electron−hole $(e^- h^+)$ pairs in the 400−800 nm range.[42] In the case of the MFO, the emission peak was observed at 595 nm. While for pure NiO and emission, a peak at 633.4 nm at a certain excitation wavelength has been found. The intense PL peak intensity for NiO indicates the quick rate of charge carrier recombination, but the rapid decline in the PL intensity for NCs indicates their low recombination rate. The decrease in PL intensity is linearly correlated with the suppression of this recombination of charges.[43] The life of the light-induced carriers is extended due to the low recombining rate of the composite materials, which improves the optical performance of the photocatalytic material. By increasing the proportion of MFO in NiO lattice, the greater separation in heterojunction increases O_2 vacancies and the formation of Fermi levels inside the CB and VB.[15]

3.6. Magnetic Properties. VSM analysis was used to record the magnetic properties of transition metal oxide NiO, spinel MFO, and NiO/MFO(1−4) NCs at room temperature for use in wastewater treatment.[30] The findings of hysteresis are listed in Figure 7. As observed, the symmetrical S-shaped magnetization curves of the pure NiO, MFO, and NCs samples NiO/MFO(1−4) indicated their nanoscale dimensions and superparamagnetic properties.[44] Both NiO and MFO nanoparticles have magnetic saturation (M_s) values of 42.7 and 60.2 emu/g, respectively. The M_s values for NiO/MFO(1−4) NCs are 29.9, 24.3, 16.4, and 12.6 emu/g, respectively. Pure MFO shows the highest values of saturation magnetization (M_s), coercivity (H_c), and remnant magnetization (M_r) whereas a significant variation in magnetization was noticed with the addition of NiO in NCs. This drop in magnetization might be associated with the nonmagnetic nature of NiO at 300 K, which, on increasing its level in NC materials, decreases their M_s.[45] The NCs with magnetic behavior have benefits because they may be utilized for subsequent applications and can be readily separated from the liquid by applying an external magnetic field after application.[46] Different parameters such as magnetic saturation (M_s), remanence (M_r), and coercivity (H_c) are given in Table 2.

3.7. Bandgap Analysis. The resulting samples were examined by DRS UV−Vis to determine the optical characteristics.[30] The diffused UV−Vis reflection spectra (DRS) of NiO, MFO, and NiO/MFO(1−4) NCs are shown in Figure 8a. The absorbing edge for pure NiO is below 350 nm, whereas the spectra of MFO show considerable adsorption intensity in the

Table 2. Hysteresis Loop Measurement of NiO, MFO, and Nanocomposite NiO/MFO(1−4)

material	magnetic saturation (M)	remanence (M_r)	coercivity (H_c)
MFO	60.2	17.6	−1109
NiO	42.7	9.5	−1197
NiO/MFO-1	29.9	6.6	−1101
NiO/MFO-2	24.3	5.1	−1022
NiO/MFO-3	16.4	4.9	−970
NiO/MFO-4	12.6	3.1	−911

broad visible light area from 400 to 850 nm. The optical band gap of synthesized NiO and MFO were 3.6 and 1.4 eV, respectively. All the NCs NiO/MFO(1−4) have band gap values at 2.6, 2.2, 1.8, and 1.6 (eV), respectively, as shown in Figure 8b. In composite materials, a significant decline in the level of E_g was observed. It indicates that the introduction of MFO decreases the band gap of NiO. Moreover, the band gap of NCs shifts to a lower value, which is due to the electronic coupling.[47] The optical bandgap may be significantly impacted by additional factors such as structural strain, variations in average crystallite size, or surface area/volume.[48] The energy of the band gap was calculated using.

$$a = \frac{(hv - E_g)^{n/2}}{hv} \tag{5}$$

The absorbance coefficient, mode of transmission, band gap energy, Planck's constant, and frequency of the incoming photon are represented by the variables α, n, E_g, h, and v, respectively. It may be inferred that increasing the quantity of ferrite in the composites would enhance their capacity to absorb light from the ultraviolet to the visible spectrum. Reduced band gap energy shows that the materials could be used for photocatalysis.

3.8. Photoelectrochemical Analysis. In order to provide strong evidence for the separation and transfer behavior of photogenerated electrons and holes in composite materials, photoelectrochemical measurements of pure NiO, MFO, and composite NiO/MFO(1−4) were carried out. Electrochemical impedance spectroscopy (EIS) was performed to evaluate the interface charge transfer resistance, indirectly indicating the separation efficiency of photogenerated charges.[49] The lower diameter of the EIS curve of a material offers lower electrical resistance but a relative higher-charge transferring rate. Thus,
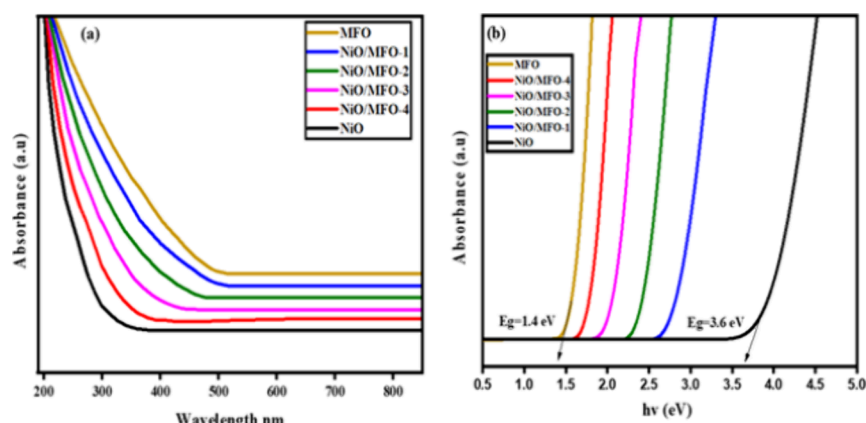
Figure 8. (a) UV−visible diffuse reflectance spectra and (b) Tauc's plot of NiO, MFO, and nanocomposite NiO/MFO(1−4).
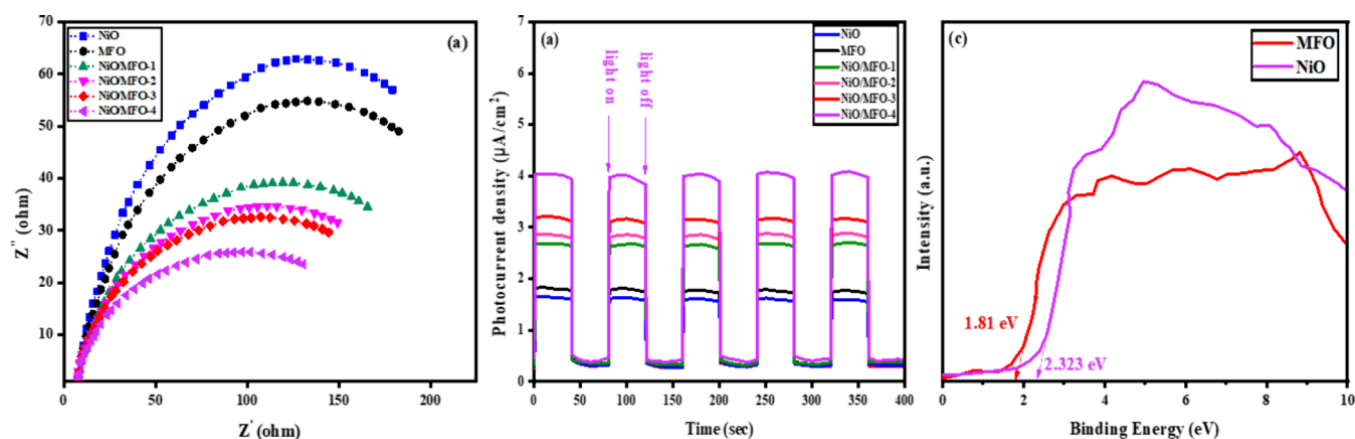

Figure 9. (a) EIS spectra of pure NiO, MFO and composites NiO/MFO(1−4), (b) transient photocurrent response of pure NiO, MFO, and composites NiO/MFO(1−4), and (c) valence band XPS spectra of NiO and MFO.

the obtained lower diameter of NiO/MFO-4 photocatalyst indicated its improved charge transfer ability in aqueous medium (Figure 9a). Figure 9b shows the transient photo-current response of pure NiO, MFO, and NiO/MFO(1−4) composites measured for five on/off cycles of simulated solar illumination. Generally, pure NiO and MFO exhibit very small photocurrent, which means that their photoexcited electrons and holes recombine very rapidly.[50] When the light is turned on, the photocurrent density of pure NiO and MFO is about 1.63 and 1.86 ($\mu A\ cm^{-2}$), while the photocurrent density of NiO/MFO(1−4) is about 2.67, 2.86, 3.21, and 4.03 ($\mu A\ cm^{-2}$), respectively. This means that the separation and transfer of photogenerated electrons and holes of the NiO/MFO-4 composite is more rapid and efficient than that of pure NiO and MFO.[51] By comparison of the optical and photoelectrochemical properties, the high-efficiency photo-generated charge separation and better electron flow of the composite are determined, indicating that the composite may exhibit higher PCA. To completely identify the construction of heterostructure, the valence and CB positions of NiO and MFO were calculated through empirical relations shown in eqs 6 and 7.[52]

$$E_{VB} = X - E_e + 0.5 E_g \qquad (6)$$

$$E_{CB} = E_{VB} - E_g \qquad (7)$$

where, X represents absolute electronegativity (i.e., geometric mean of the absolute electronegativity of constituent atoms) of

semiconducting material and is also referred to as the arithmetic mean of first ionization potential and electron affinity, while E_{VB}, E_{CB}, and E_c are the valence and CB potentials and free electron's energy on the hydrogen scale (∼ 4.5 eV). From X values of pure NiO and MFO, their VB potentials were calculated as 2.323 and 1.81 eV vs NHE, respectively, which were in good agreement with VB XPS spectra[53] (Figure 9c). From VB potential and E_g values, the CB potential for MFO and NiO were determined as −0.21 and 0.41 eV, respectively.

3.9. PCA. *3.9.1. Photodegradation of CR Dye.* The PCA of NiO/MFO-1 and NiO/MFO-4 was compared with that of pure NiO and MFO for the degradation of CR dye under visible light irradiation. Figure 10 shows the CR dye's UV−visible absorption spectrum when applied to pure and NCs NiO/MFO(1−4) materials. The degrading activity of pure and NCs against CR dye is given in the form of A_t/A_o in Figure 11, where A_o is the concentration of dye at time $t = 0$ and A_t is the concentration for time interval t.

UV−visible spectra revealed that NCs NiO/MFO-1, NiO/MFO-2, NiO/MFO-3, and NiO/MFO-4 catalysts are much more efficient and show 83.2, 85.6, 87.2, and 91.62% removal of CR dye, respectively, while the pure NiO and MFO show 68.24 and 70.12%, respectively. The robust catalytic efficiency of NCs NiO/MFO-4 might be ascribed to its wider light absorption range that assists the trapping of e⁻/h⁺ pair to hinder the recombination process. On the other hand, the lower degradation efficiency of pure NiO and MFO can be
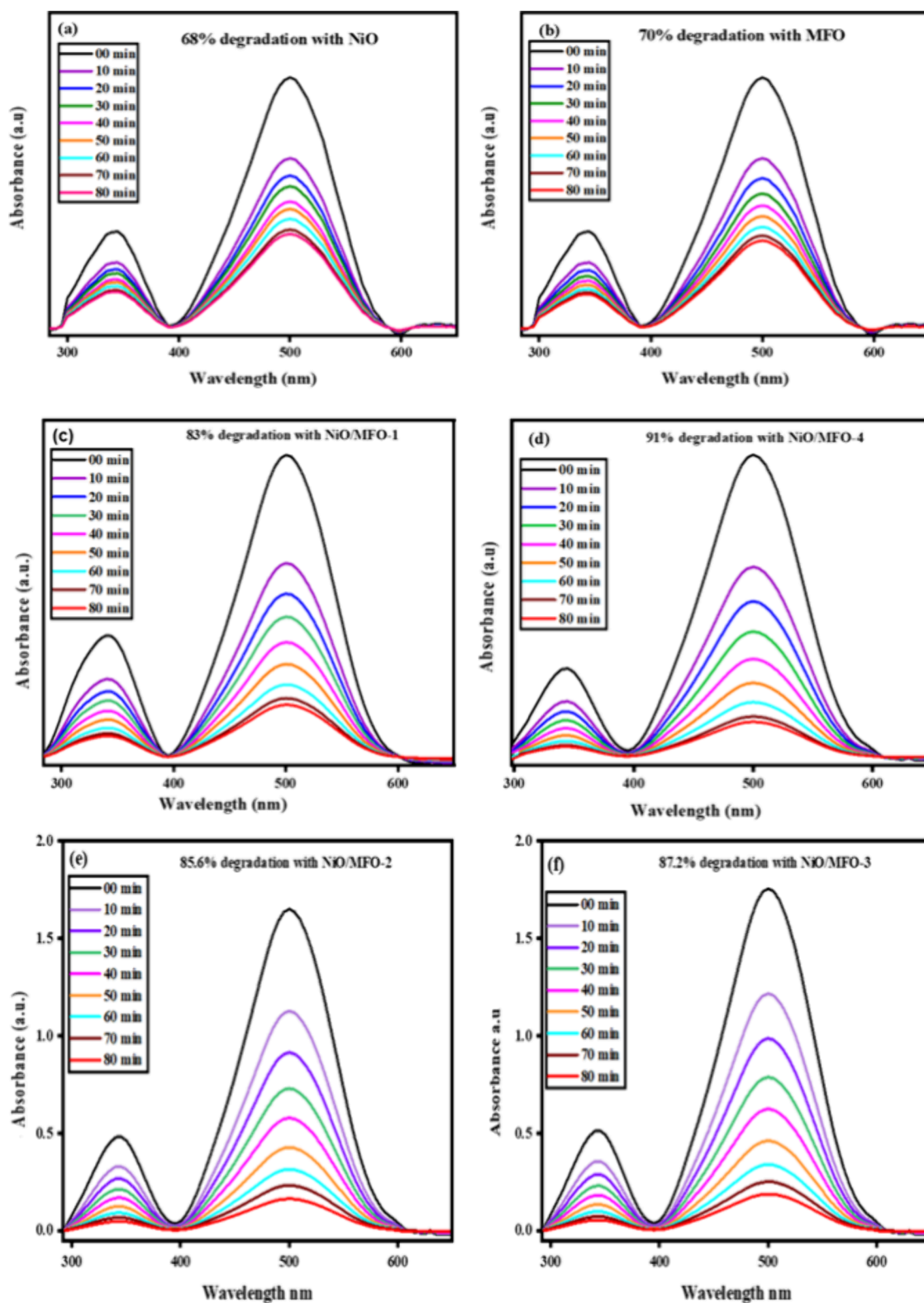
Figure 10. CR dye degradation (a, b) NiO, MFO, and (c−f) NiO/MFO(1−4) photocatalysts under visible light irradiation.

attributed to the fast recapturing of charge carriers induced on their surface which drops the photocatalytic efficiency.

3.9.2. Degradation Kinetics. To understand the kinetics of photo removal of CR dye over NiO, MFO, NiO/MFO-1, and NiO/MFO-4 photocatalysts, the k (rate constant) for dye degradation was calculated using the Langmuir−Hinshelwood equation, as given in eq 8.[54,55]

$$k_{app} = -\ln \frac{A_t}{A_o} \tag{8}$$

The slope of the curve was used to calculate the k_{app} value for the photodegradation reaction (PDR). Linear fitting of data showed that photo removal of CR follows pseudo-first-order kinetics over all four photocatalysts, as shown in Figure 11.
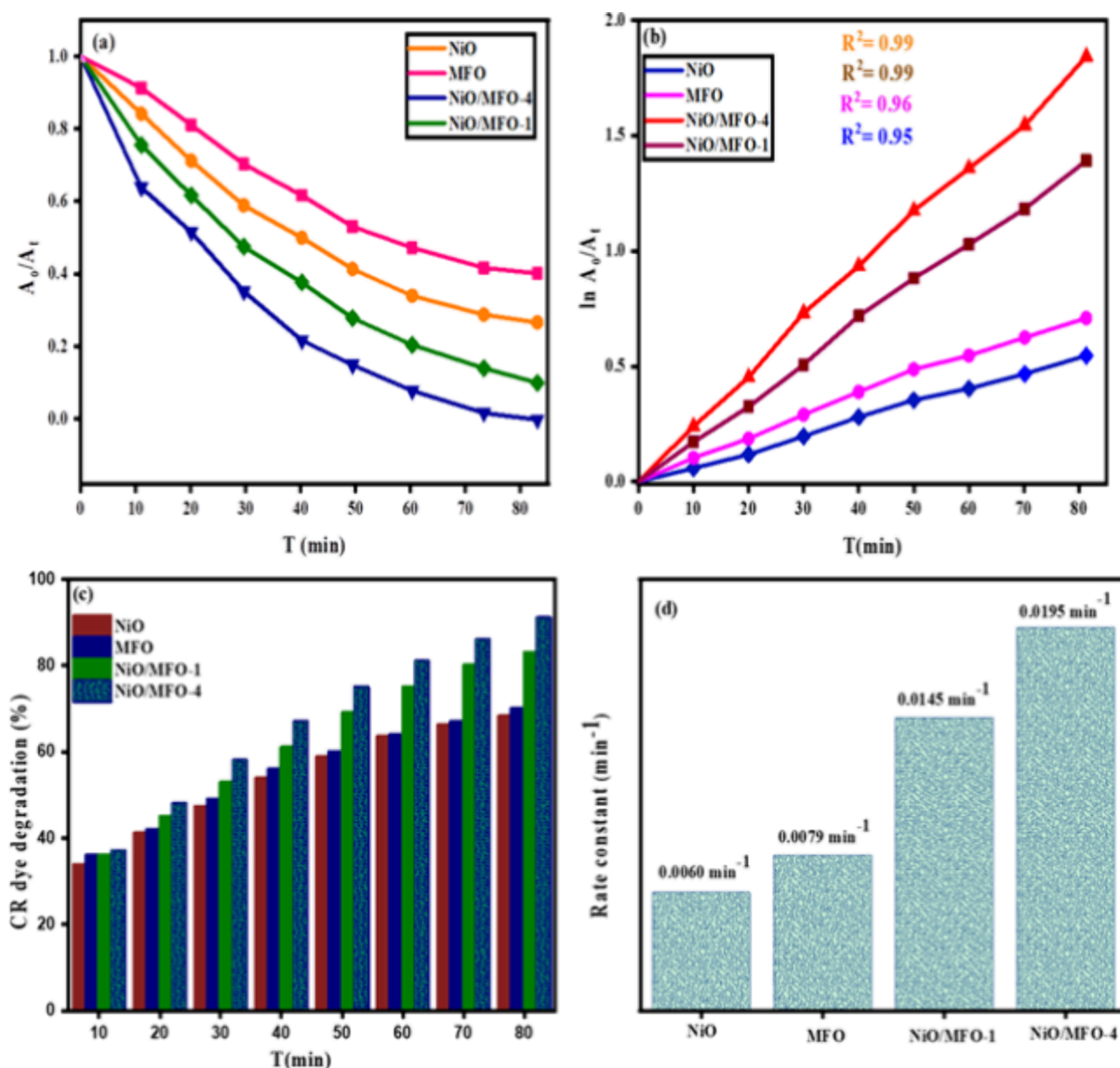
Figure 11. (a) Rate of degradation, (b) kinetics, (c) % degradation, and (d) rate constant for degradation of CR dye over NiO, MFO, NiO/MFO-1, and NiO/MFO-4 photocatalysts under visible light irradiation.

Under visible light irradiation, k_{app} for degradation of CR dye over pure NiO and MFO catalysts were 0.0060 and 0.0079 min^{-1}, respectively, but the k_{app} for NCs NiO/MFO-1 and NiO/MFO-4 catalysts were 0.0145 and 0.0195 min^{-1}, respectively. We evaluated the photocatalytic performance of our manufactured NC catalyst with closely related literature, and it was shown that modified catalysts had better dye degradation efficiency than pure materials (Table 3).

3.9.3. Scavenging Study. To understand the probable mechanism of photodegradation of dye, active species trapping experiments were conducted by studying the charge-transfer mechanism and identifying the primary radicals responsible for the photodegradation of the CR dye. Three different trapping agents isopropanol, EDTA, and AgNO$_3$ were utilized as scavengers to trap $HO^{\bullet}$, h^{+}, and e^{-}, respectively. The decolorization of CR dye without any scavenger was 91.6%, while in the presence of EDTA, a crucial decrease in CR degradation was noticed, which showed the crucial function of h^{+} in CR degradation under irradiation. With AgNO$_3$, the degradation of CR was significantly reduced, showing that

Table 3. Photocatalytic Degradation of CR Dye over Pure and NC Catalysts and Some Previously Reported Catalysts

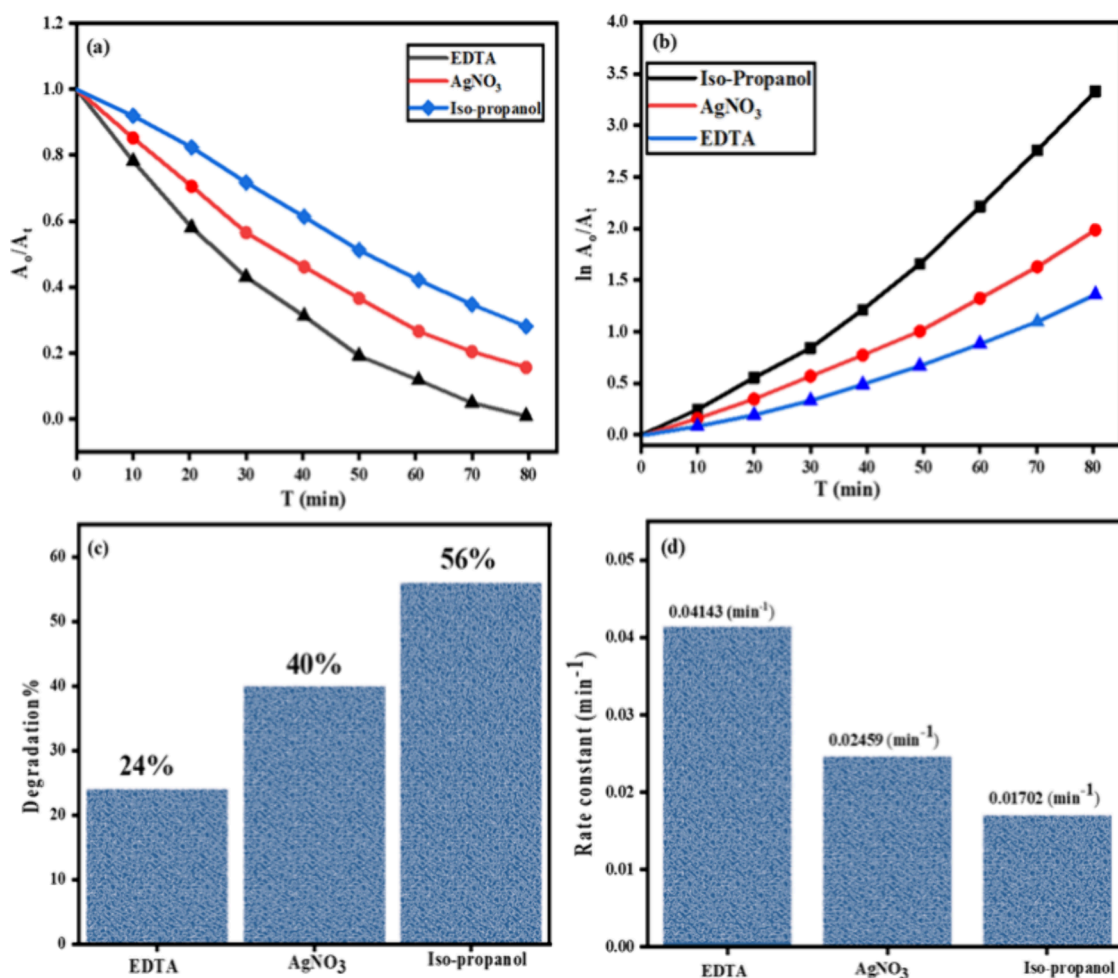| photocatalyst	dyes	degradation (%)	time (min)	k_{app}	references
g-C$_3$N$_4$	CR	13.0	120		56
ZnFeCoO	CR	81.8	60		57
ZnO-CeO$_2$–Yb$_2$O$_3$	CR	78.0	40		58
ZnO-V$_2$O$_5$–WO$_3$	CR	67.0	80		59
CuO–MgO–ZnO	MB, MO, RhB, CR	75.9–98.8	120		60
Ag-CdSe/GO@CA	MG	94	25		61
Cds@MsO$_2$	MB	80	30		62
MFO	CR	70.12	80	0.0060	this study
NiO	CR	68.24	80	0.0079	this study
NiO/MFO-1	CR	83.2	80	0.0145	this study
NiO/MFO-4	CR	91.6	80	0.0195	this study

Figure 12. (a, b) Kinetics of CR dye with different scavenging agents. (c) Degradation (%) of CR dye with scavengers for NC. (d) Rate constant of CR dye with scavengers for NiO/MFO-4 NCs.
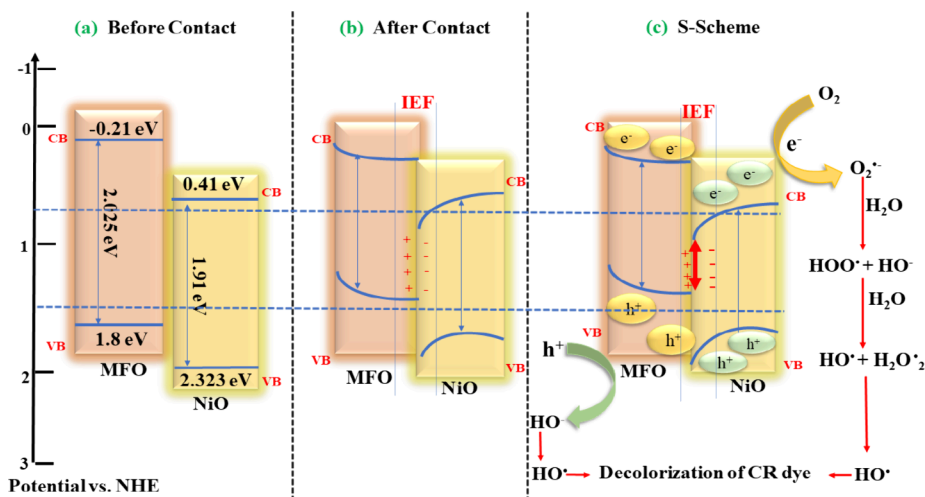

Figure 13. Photocatalytic mechanism of CR dye degradation over NiO/MFO nanocomposite.

photoexcited electrons also play a significant role in the removal of dye over the NC catalyst. However, with isopropanol, no significant decline in CR degradation was observed, demonstrating that HO$^\bullet$ did not directly contribute to the photodegradation process. The percentage of dye degradation was decreased for the above-mentioned scavenging agents to 24, 40, and 56% with a rate constant of 0.041,

0.02459, and 0.01702 min^{-1}, as shown in Figure 12, respectively. The results demonstrated that the holes (h$^+$) are the main active species and play a major role in the photocatalysis of CR dye. While the HO$^\bullet$ radicals have a minor part in photodegradation utilizing NiO/MFO-4 as the photocatalyst, the e$^-$ also plays a significant role in CR
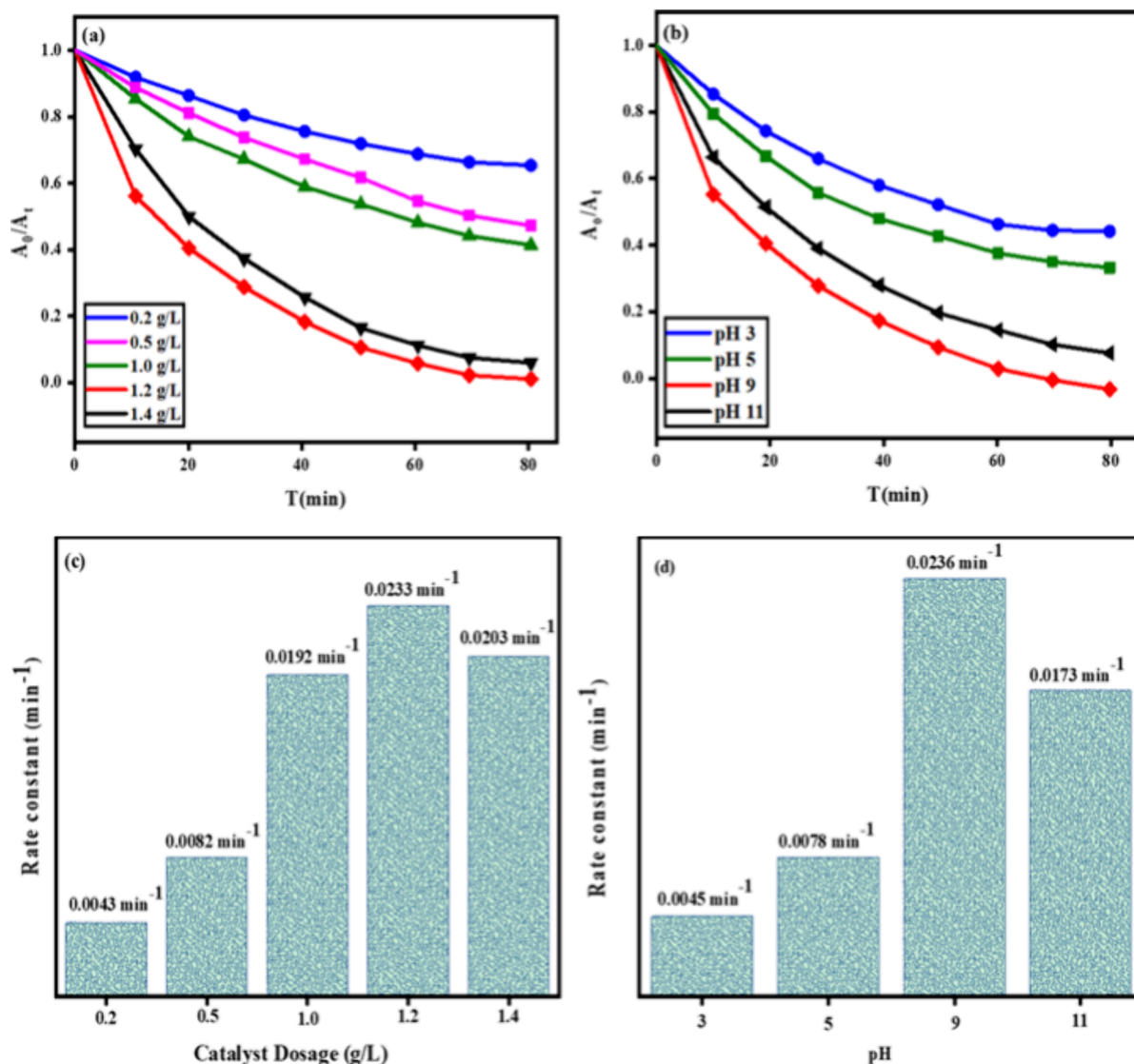
Figure 14. Effect of reaction parameters on the degradation of CR dye: (a, b) catalyst dosage and pH and (c, d) rate constant.

degradation. The sequence of effect of scavengers involved in the degradation of CR dye was observed as $h^+ > e^- > HO^•$.

3.9.4. Mechanism of Dye Photocatalytic Degradation. The S-scheme photocatalytic mechanism for dye degradation is proposed[63−65] and illustrated in Figure 13. A possible pathway for photodecolorization of CR under visible irradiation can be suggested. When a semiconducting material absorbs radiation $\geq E_g$, the valence band electrons (eVB) get excited to the CB creating a hole thus generating an e^-/h^+ pair at its surface that helps in conduction of the redox process to degrade the adsorbed dye. The PCA of a semiconductor-aided photocatalyst is considered to be essentially dependent on the formation, separation, and transfer of light-induced e^--h^+ pairs. Here, the separation of such charge carriers was made possible in large part by n-p type NiO/MFO nanocomposites. Eventually, an internal field where a lower barrier switches to exist may aid in the separation and migration of light-induced carriers. This might significantly lower the probability of an electron–hole rejoining because a substantial amount of active e^- and h^+ on the NiO/MFO4 interface can take part in the dye's photodriven redox process. The above results can be correlated to PL observations where separation as well as

rejoining of photoinduced charge carriers depends directly on PL peak intensity. In the case of composite material, the PL emission signal becomes considerably weaker after heterostructure formation with NiO; this determines the notable restriction of this recombination. Active electrons on CB of NiO might be engaged by O_2 adsorbed on its surface to form $^-•O_2$ that through undergoing several reactions ultimately changes to hydroxyl $OH^•$ radicals. These radicals were then directly involved in the removal of dye effluent from the reacting mixture under irradiation. Besides, active holes on VB of MFO may oxidize also the organic dye owing to its effective oxidizing power (Figure 13).

According to the aforementioned findings, the potential improvement in PCA of NiO/MFO4 nanocomposite over that of pure MFO and NiO may be ascribed to first, the presence of a synergistic interaction between MFO and NiO that results in effective separation of photogenerated electron–hole pairs; and second, the optimized parameters high crystallinity, reduced energy band gap, voids pores, and charge carrier recombination hindrance for the NiO/MFO4 nanocomposites have superior PCA when compared to synthetically produced pure NiO and MFO.

3.10. Effect of Process Variables on Dye Degradation.

In the current study, the effect of reaction parameters like catalyst dosage and pH were evaluated during CR degradation by NiO/MFO-4 nanocomposite for meeting the need for practical applications.

3.10.1. Catalyst Dosage. The effect of NiO/MFO4 catalyst dose in 0.2−1.4 g/L range (at neutral pH), on photo-decolorization of CR dye, was investigated for 80 min. On increasing the catalyst amount, the % removal of dye was increased from 91.6 to 96.3% until 1.2 g/L of catalyst dosage, beyond this, it was decreased to 92.7% at 1.4 g/L dose of catalyst (Figure 14a). This observation can be explained on the base of the availability of active sites on the surface of the photocatalyst for the adsorption of dye particles that may increase on increasing the catalyst dose in the reaction mixture.[66] Moreover, the drop in removal efficiency above 1.4 g/L might be associated with several factors such as aggregation of catalyst particles, formation of suspension in the reaction mixture, and reduction in irradiation diffusion in an aqueous medium.[67] Furthermore, the pseudo-first-order kinetics model was followed by the kinetics of CR degradation with rate constants of 0.0043, 0.0082, 0.0192, 0.0233, and 0.0203 (min^{-1}) at catalyst concentrations of 0.2, 0.5, 1.0, 1.2, and 1.4 (g/L), respectively (Figure 14c). However, the best catalyst dose of 1 g/L was selected for further experiments after taking into account both the catalytic outcome and the operational cost.

3.10.2. Effect of pH. One of the most important factors affecting the catalyst's PCA is its initial pH. This is explained by the significant effects of the photocatalytic process on variables like the molecular and surface charges of the material, the adsorption of organic pollutants onto the surface of the photocatalyst, and the concentration of hydroxyl radicals ($^\bullet$OH) in the aqueous solution.[68,69] Figure 14b shows the data that we obtained from our analysis of the CR dye removal process in the pH range of 3−11. After an 80 min reaction, the removal efficiencies of CR were determined to be 65.4, 70.3, 91.8, and 67.1% under initial pH values of 3, 5, 9, and 11, respectively. Furthermore, Figure 13d shows the reaction rate constants at various pH values. At pH 9, the highest degradation rate constant $(0.0236 \ min^{-1})$ was observed. The removal of CR dye was found to be negatively impacted by the higher leaching concentration of Ni^{2+} under acidic conditions, which is why there was a decrease in CR removal efficiency at pH 3 and pH 11. The degradation of CR dye was considerably impeded at pH 11 by the depletion of $HO^\bullet$ as a result of its reaction with OH^-.[69] At pH 9, the removal efficiency of CR dye was greatly enhanced which might be due to the zero-point charge (pH_{zpc}) present on the surface of the catalyst.[70]

3.11. Recycling and Reusability Tests.

The reusability and structural stability of the NiO/MFO-4 photocatalyst for practical applications were evaluated for four consecutive cyclic runs under the same exposure time. Used NiO/MFO-4 NCs were recollected from an aqueous medium through an applied magnetic field and were dried at 50 °C. Results show that the % removal of dye for the second, third, and fourth cycle was dropped to 81, 77, and 75% respectively (Figure S1). Following each run in the recycling studies, a progressive decline in the nanocomposite (NC) PCA was noted. Catalyst loss, which results from the deactivation of active sites, separation during subsequent cycles, and the aggregation or leaching of the photocatalyst's surface caused by repeat heat treatments, can be blamed for this decrease.[71] The XRD analysis was used to determine the phase stability of reused NiO/MFO4 catalyst (Figure S2). The distinctive peaks at the relevant 2-theta angle were retained in the diffraction spectra of the catalyst that was utilized, indicating that it was structurally stable without showing any secondary phase. Relatively low intensity peaks were observed in the case of reused catalyst, which was possibly due to a minor loss in the amount of catalyst amount recovered. Outcomes indicated that NiO/MFO4 nanocomposites exhibited good recoverability and phase stability, which suggest their practical utility in the economical removal of dye from industrial discharge water.

4. CONCLUSIONS

Pure NiO, $MnFe_2O_4$ (MFO), and NiO/MFO(1−4) NCs in various mole ratios were fabricated by ultrasonication method and studied for their PCA toward the removal of CR dye under solar irradiation. The NiO/MFO-4 nanocomposite demonstrated better PCA to degrade CR dye at 91.6% under visible light irradiation in comparison to pure (NiO and MFO) materials. This better photoactivity can be associated with enhanced active surface area of NiO/MFO-4, as shown by the large crystallite size of NCs that facilitated more adsorption of dye on its surface. The SEM photograph demonstrates an agglomerated, nonuniform structure with pores and spaces. Bending and stretching modes in fabricated materials were confirmed using FT-IR. The optical band gap and PL of NCs decrease with the addition of ferrites, which confirms the low recombination rate of NCs. NiO/MFO-4 NCs were separated quickly from the aqueous solution owing to its good magnetic moment. Its superior catalytic activity was still preserved, with a minor decline after four successive cycles of degradation of CR dye. The catalyst dosage of 1.2 g/L and pH 9 show maximum degradation of CR dye under visible light irradiation with a rate constant of 0.0233 and 0.0236 min^{-1}, respectively. Scavenging results showed that h^+ and e were the chief active species in the removal of the dye over NiO/MFO-4 NCs. Ultimately, novel NiO/MFO-4 nanohybrids have superior catalytic activity and robust magnetic separability and may find their potential applicability in the removal of dyes from wastewater.

■ ASSOCIATED CONTENT

Ⓢ Supporting Information

The Supporting Information is available free of charge at https://pubs.acs.org/doi/10.1021/acsomega.3c09637.

Stability and reusability run for the NCs photo-catalyst and XRD patterns of used catalyst after removal of CR dye under solar irradiation (PDF)

■ AUTHOR INFORMATION

Corresponding Authors

Ismat Bibi − *Institute of Chemistry, The Islamia University of Bahawalpur, Bahawalpur 63100, Pakistan*; Email: drismat@iub.edu.pk

Norah Alwadai − *Department of Physics, College of Sciences, Princess Nourah bint Abdulrahman University, Riyadh 11671, Saudi Arabia*; Email: nmalwadai@pnu.edu.sa

Munawar Iqbal − *Department of Chemistry, Division of Science and Technology, University of Education, Lahore 54770, Pakistan*; ⓞ orcid.org/0000-0001-7393-8065; Email: bosalvee@yahoo.com

Authors

Muhammad Amjad − *Institute of Chemistry, The Islamia University of Bahawalpur, Bahawalpur 63100, Pakistan*

Farzana Majid − *Department of Physics, University of the Punjab, Lahore 54590, Pakistan*

Kashif Jilani − *Department of Biochemistry, University of Agriculture, Faisalabad 38000, Pakistan*

Misbah Sultan − *School of Chemistry, University of the Punjab, Lahore 54590, Pakistan*

Qasim Raza − *Institute of Chemistry, The Islamia University of Bahawalpur, Bahawalpur 63100, Pakistan*

Aamir Ghafoor − *Institute of Chemistry, The Islamia University of Bahawalpur, Bahawalpur 63100, Pakistan*

Arif Nazir − *Department of Chemistry, University of Lahore, Lahore 54000, Pakistan;* ⊙ orcid.org/0000-0002-9412-6100

Complete contact information is available at:
https://pubs.acs.org/10.1021/acsomega.3c09637

Notes

The authors declare no competing financial interest.

■ REFERENCES

(1) Fatima, S.; Iqbal, M.; Bhatti, H. N.; Iqbal, M.; Alwadai, N.; Al Huwayz, M.; Nazir, A. Synthesis of Oval-Shaped Bi2Al4O9 Nanoparticles and Their Applications for the Degradation of Acid Green 25 and as Fuel Additives. *ACS Omega* **2023**, *8* (34), 30868−30878.

(2) Chouke, P. B.; Dadure, K. M.; Potbhare, A. K.; Bhusari, G. S.; Mondal, A.; Chaudhary, K.; Singh, V.; Desimone, M. F.; Chaudhary, R. G.; Masram, D. T. Biosynthesized δ-Bi2O3 Nanoparticles from Crinum viviparum Flower Extract for Photocatalytic Dye Degradation and Molecular Docking. *ACS omega* **2022**, *7* (24), 20983−20993.

(3) Dagde, K.; Ikenyiri, P.; Yorpah, P. Application of Gure modified clay for adsorption of heavy metals in polluted underground water. *Chem. Int.* **2023**, *9* (3), 94−103.

(4) Alkherraz, A. M.; Elsherif, K. M.; Blayblo, N. A. Safranin adsorption onto Acasia plant derived activated carbon: Isotherms, thermodynamics and kinetic studies. *Chem. Int.* **2023**, *9* (4), 134−145.

(5) Abid, H.; Amanat, A.; Ahmed, D.; Qamar, T. Adsorption efficacy of Carissa opaca roots residual biomass for the removal of copper from contaminated water. *Chem. Int.* **2023**, *9* (1), 1−7.

(6) Abbas, N.; Abbas, A.; Irfan, M.; Khan, M. H.; Ayesha. Evaluating key parameters for developing a sustainable solid waste management plan in Lahore-China scheme. *Chem. Int.* **2023**, *9* (3), 120−127.

(7) Ukpaka, C. P.; Ugiri, A. C. Biodegradation kinetics of petroleum hydrocarbon in soil environment using Mangnifera indica seed biomass: A mathematical approach. *Chem. Int.* **2022**, *8* (2), 77−88.

(8) Abbas, N.; Butt, M. T.; Ahmad, M. M.; Deeba, F.; Hussain, N. Phytoremediation potential of Typha latifolia and water hyacinth for removal of heavy metals from industrial wastewater. *Chem. Int.* **2021**, *7*, 103−111.

(9) Djehaf, K.; Bouyakoub, A. Z.; Ouhib, R.; Benmansour, H.; Bentouaf, A.; Mahdad, A.; Moulay, N.; Bensaid, D.; Ameri, M. Textile wastewater in Tlemcen (Western Algeria): Impact, treatment by combined process. *Chem. Int.* **2017**, *3* (4), 414−419.

(10) Khaliq, N.; Bibi, I.; Majid, F.; Arshad, M. I.; Ghafoor, A.; Nazeer, Z.; Ezzine, S.; Alwadai, N.; Nazir, A.; Iqbal, M. Mg1-xNixFe2-xCrxO4 synthesis via hydrothermal route: Effect of doping on the structural, optical, electrical, magnetic and photocatalytic properties. *Results in Physics* **2022**, *43*, No. 106059.

(11) Nazeer, Z.; Bibi, I.; Majid, F.; Kamal, S.; Ghafoor, A.; Ali, A.; Kausar, A.; Elqahtani, Z. M.; Alwadai, N.; Iqbal, M. Microemulsion synthesis of Ga and Sr doped BiFeO3 nanoparticles and evaluation of their ferroelectric, optical, dielectric and photocatalytic properties. *Physica B: Condensed Matter* **2023**, *657*, No. 414788.

(12) Ahmad, B.; Khan, M. I.; Naeem, M. A.; Alhodaib, A.; Fatima, M.; Amami, M.; Al-Abbad, E. A.; Kausar, A.; Alwadai, N.; Nazir, A.; et al. Green synthesis of NiO nanoparticles using Aloe vera gel extract and evaluation of antimicrobial activity. *Mater. Chem. Phys.* **2022**, *288*, No. 126363.

(13) Mohsin, M.; Bhatti, I. A.; Ashar, A.; Mahmood, A.; ul Hassan, Q.; Iqbal, M. Fe/ZnO@ceramic fabrication for the enhanced photocatalytic performance under solar light irradiation for dye degradation. *J. Mater. Res. Technol.* **2020**, *9*, 4218−4229.

(14) Wang, X.; Wang, A.; Ma, J. Visible-light-driven photocatalytic removal of antibiotics by newly designed C3N4@ MnFe2O4-graphene nanocomposites. *Journal of hazardous materials* **2017**, *336*, 81−92.

(15) Shekofteh-Gohari, M.; Habibi-Yangjeh, A.; Abitorabi, M.; Rouhi, A. Magnetically separable nanocomposites based on ZnO and their applications in photocatalytic processes: a review. *Critical Reviews in Environmental Science and Technology* **2018**, *48* (10−12), 806−857.

(16) Raza, Q.; Bibi, I.; Majid, F.; Kamal, S.; Ata, S.; Ghafoor, A.; Arshad, M. I.; Al-Mijalli, S. H.; Nazir, A.; Iqbal, M. Solar light-based photocatalytic removal of CV and RhB dyes using Bi and Al doped SrFe12O19 NPs and antibacterial properties. *Journal of Industrial and Engineering Chemistry* **2023**, *118*, 469−482.

(17) Yao, Y.; Cai, Y.; Lu, F.; Wei, F.; Wang, X.; Wang, S. Magnetic recoverable MnFe2O4 and MnFe2O4-graphene hybrid as heterogeneous catalysts of peroxymonosulfate activation for efficient degradation of aqueous organic pollutants. *Journal of hazardous materials* **2014**, *270*, 61−70.

(18) Nausheen, S.; Bhatti, H. N.; Arif, K.; Nisar, J.; Iqbal, M. Native clay, MnFe2O4/clay composite and bio-composite efficiency for the removal of synthetic dye from synthetic solution: column versus batch adsorption studies. *DESALINATION AND WATER TREATMENT* **2020**, *187*, 219−231.

(19) Kanwal, A.; Bhatti, H. N.; Iqbal, M.; Noreen, S. Basic dye adsorption onto clay/MnFe2O4 composite: a mechanistic study. *Water Environment Research* **2017**, *89* (4), 301−311.

(20) Rahimi, R.; Bozorgpour, M.; Rabbani, M. Synthesis of Fe-doped Nickel oxide nanostructures via a simple mechanochemical route and its application for photocatalytic removing of MB; In *17th International Electronic Conference on Synthetic Organic Chemistry*, 2013.

(21) Zeng, H.; Rice, P. M.; Wang, S. X.; Sun, S. Shape-controlled synthesis and shape-induced texture of MnFe2O4 nanoparticles. *J. Am. Chem. Soc.* **2004**, *126* (37), 11458−11459.

(22) Mustapha, S.; Ndamitso, M.; Abdulkareem, A.; Tijani, J.; Shuaib, D.; Mohammed, A.; Sumaila, A. Comparative study of crystallite size using Williamson-Hall and Debye-Scherrer plots for ZnO nanoparticles. *Advances in Natural Sciences: Nanoscience and Nanotechnology* **2019**, *10* (4), No. 045013.

(23) Shah, A. H.; Rather, M. A. Effect of calcination temperature on the crystallite size, particle size and zeta potential of TiO2 nanoparticles synthesized via polyol-mediated method. *Materials Today: Proceedings* **2021**, *44*, 482−488.

(24) Andrade, A. B.; Ferreira, N. S.; Valerio, M. E. Particle size effects on structural and optical properties of BaF 2 nanoparticles. *RSC Adv.* **2017**, *7* (43), 26839−26848.

(25) Murty, B.; Shankar, P.; Raj, B.; Rath, B.; Murday, J.; Murty, B.; Shankar, P.; Raj, B.; Rath, B.; Murday, J.Unique properties of nanomaterials; In *Textbook of nanoscience and nanotechnology*; Springer: Berlin, Heidelberg, 2013, pp. 29−65. DOI:.

(26) Mallakpour, S.; Hatami, M.; Hussain, C. M. Recent innovations in functionalized layered double hydroxides: Fabrication, character-

ization, and industrial applications. *Adv. Colloid Interface Sci.* **2020**, *283*, No. 102216.

(27) Dippong, T.; Levei, E.-A.; Lengauer, C. L.; Daniel, A.; Toloman, D.; Cadar, O. Investigation of thermal, structural, morphological and photocatalytic properties of CuxCo1-xFe2O4 (0≤ x≤ 1) nanoparticles embedded in SiO2 matrix. *Mater. Charact.* **2020**, *163*, No. 110268.

(28) Prasanna Kumar, J. B.; Ramgopal, G.; Vidya, Y.; Anantharaju, K.; Prasad, B. D.; Sharma, S.; Prashantha, S.; Premkumar, H.; Nagabhushana, H. Bio-inspired synthesis of Y2O3: Eu3+ red nanophosphor for eco-friendly photocatalysis. *Spectrochim. Acta, Part A* **2015**, *141*, 149−160.

(29) John, K. I.; Adenle, A. A.; Adeleye, A. T.; Onyia, I. P.; Amune-Matthews, C.; Omorogie, M. O. Unravelling the effect of crystal dislocation density and microstrain of titanium dioxide nanoparticles on tetracycline removal performance. *Chem. Phys. Lett.* **2021**, *776*, No. 138725.

(30) Ma, Q.; Zhang, H.; Zhang, X.; Li, B.; Guo, R.; Cheng, Q.; Cheng, X. Synthesis of magnetic CuO/MnFe2O4 nanocompisite and its high activity for degradation of levofloxacin by activation of persulfate. *Chemical Engineering Journal* **2019**, *360*, 848−860.

(31) Mary Jacintha, A.; Manikandan, A.; Chinnaraj, K.; Arul Antony, S.; Neeraja, P. Comparative studies of spinel MnFe2O4 nanostructures: structural, morphological, optical, magnetic and catalytic properties. *J. Nanosci. Nanotechnol.* **2015**, *15* (12), 9732−9740.

(32) Alagiri, M.; Ponnusamy, S.; Muthamizhchelvan, C. Synthesis and characterization of NiO nanoparticles by sol−gel method. *Journal of Materials Science: Materials in Electronics* **2012**, *23*, 728−732.

(33) Varshney, D.; Dwivedi, S. Synthesis, structural, Raman spectroscopic and paramagnetic properties of Sn doped NiO nanoparticles. *Superlattices Microstruct.* **2015**, *86*, 430−437.

(34) Kanagesan, S.; Aziz, S. B. A.; Hashim, M.; Ismail, I.; Tamilselvan, S.; Alitheen, N. B. B. M.; Swamy, M. K.; Rao, Purna Chandra; B. Synthesis, characterization and in vitro evaluation of manganese ferrite (MnFe2O4) nanoparticles for their biocompatibility with murine breast cancer cells (4T1). *Molecules* **2016**, *21* (3), 312.

(35) Zipare, K.; Dhumal, J.; Bandgar, S.; Mathe, V.; Shahane, G. Superparamagnetic manganese ferrite nanoparticles: synthesis and magnetic properties. *J. Nanosci. Nanoeng.* **2015**, *1* (3), 178−182.

(36) Joshi, S.; Kumar, M.; Chhoker, S.; Srivastava, G.; Jewariya, M.; Singh, V. Structural, magnetic, dielectric and optical properties of nickel ferrite nanoparticles synthesized by co-precipitation method. *Journal of Molecular structure* **2014**, *1076*, 55−62.

(37) Venkataraju, C.; Paulsingh, R. FTIR and EPR studies of nickel substituted nanostructured Mn Zn ferrite. *J. Nanosci.* **2014**, *2014*, No. 815385, DOI: 10.1155/2014/815385.

(38) Bibi, I.; Muneer, M.; Iqbal, M.; Alwadai, N.; Almuqrin, A. H.; Altowyan, A. S.; Alshammari, F. H.; Almuslem, A. S.; Slimani, Y. Effect of doping on dielectric and optical properties of barium hexaferrite: photocatalytic performance under solar light irradiation. *Ceram. Int.* **2021**, *47* (22), 31518−31526.

(39) Lu, M.-L.; Lin, T.-Y.; Weng, T.-M.; Chen, Y.-F. Large enhancement of photocurrent gain based on the composite of a single n-type SnO 2 nanowire and p-type NiO nanoparticles. *Opt. Express* **2011**, *19* (17), 16266−16272.

(40) Sharifi, S.; Rahimi, K.; Yazdani, A. Highly improved supercapacitance properties of MnFe2O4 nanoparticles by MoS2 nanosheets. *Sci. Rep.* **2021**, *11* (1), 8378.

(41) Thinh, D. B.; Tien, N. T.; Dat, N. M.; Phong, H. H. T.; Giang, N. T. H.; Oanh, D. T. Y.; Nam, H. M.; Phong, M. T.; Hieu, N. H. Improved photodegradation of p-nitrophenol from water media using ternary MgFe2O4-doped TiO2/reduced graphene oxide. *Synth. Met.* **2020**, *270*, No. 116583.

(42) Alenizi, M.; Kumar, R.; Aslam, M.; Alseroury, F.; Barakat, M. Construction of a ternary g-C3N4/TiO2@ polyaniline nanocomposite for the enhanced photocatalytic activity under solar light. *Sci. Rep.* **2019**, *9* (1), No. 12091.

(43) Asiri, S.; Güner, S.; Korkmaz, A.; Amir, M.; Batoo, K.; Almessiere, M. A.; Gungunes, H.; Sözeri, H.; Baykal, A. Magneto-optical properties of BaCryFe12− yO19 (0.0≤ y≤ 1.0) hexaferrites. *J. Magn. Magn. Mater.* **2018**, *451*, 463−472.

(44) Kumar, S.; Nair, R. R.; Pillai, P. B.; Gupta, S. N.; Iyengar, M.; Sood, A. K. Graphene oxide−MnFe2O4 magnetic nanohybrids for efficient removal of lead and arsenic from water. *ACS Appl. Mater. Interfaces* **2014**, *6* (20), 17426−17436.

(45) Sharma, A.; Godara, S.; Srivastava, A. Influence of composition variation on structural, magnetic and dielectric properties of Gd3Fe5O12 (x)/MgFe2O4 (1− x) composite. *Indian Journal of Physics* **2022**, *96* (14), 4173−4184.

(46) Liu, J.; Qiao, S. Z.; Hu, Q. H.; Lu, G. Q. Magnetic nanocomposites with mesoporous structures: synthesis and applications. *Small* **2011**, *7* (4), 425−443.

(47) Munir, S.; Rasheed, A.; Zulfiqar, S.; Aadil, M.; Agboola, P. O.; Shakir, I.; Warsi, M. F. Synthesis, characterization and photocatalytic parameters investigation of a new CuFe2O4/Bi2O3 nanocomposite. *Ceram. Int.* **2020**, *46* (18), 29182−29190.

(48) Irshad, Z.; Bibi, I.; Ghafoor, A.; Majid, F.; Kamal, S.; Ezzine, S.; Elqahtani, Z. M.; Alwadai, N.; El Messaoudi, N.; Iqbal, M. Ni doped SrFe12O19 nanoparticles synthesized via micro-emulsion route and photocatalytic activity evaluation for the degradation of crystal violet under visible light irradiation. *Results in Physics* **2022**, *42*, No. 106006.

(49) Zhao, W.; Wei, Z.; Zhang, X.; Ding, M.; Huang, S.; Yang, S. Magnetic recyclable MnFe2O4/CeO2/SnS2 ternary nano-photocatalyst for photo-Fenton degradation. *Applied Catalysis A: General* **2020**, *593*, No. 117443.

(50) Jiang, Z.; Chen, K.; Zhang, Y.; Wang, Y.; Wang, F.; Zhang, G.; Dionysiou, D. D. Magnetically recoverable MgFe2O4/conjugated polyvinyl chloride derivative nanocomposite with higher visible-light photocatalytic activity for treating Cr (VI)-polluted water. *Sep. Purif. Technol.* **2020**, *236*, No. 116272.

(51) Skliri, E.; Vamvasakis, I.; Papadas, I. T.; Choulis, S. A.; Armatas, G. S. Mesoporous composite networks of linked MnFe2O4 and ZnFe2O4 nanoparticles as efficient photocatalysts for the reduction of Cr (VI). *Catalysts* **2021**, *11* (2), 199.

(52) Palanisamy, G.; Vignesh, S.; Srinivasan, M.; Venkatesh, G.; Elavarasan, N.; Pazhanivel, T.; Ramasamy, P.; Shaikh, S. F.; Ubaidullah, M.; Reddy, V. R. M. Construction of magnetically recoverable novel Z-scheme La (OH) 3/α-MnO2/MnFe2O4 photocatalyst for organic dye degradation under UV−visible light illumination. *J. Alloys Compd.* **2022**, *901*, No. 163539.

(53) Stevanović, V.; Lany, S.; Ginley, D. S.; Tumas, W.; Zunger, A. Assessing capability of semiconductors to split water using ionization potentials and electron affinities only. *Phys. Chem. Chem. Phys.* **2014**, *16* (8), 3706−3714.

(54) da Silva, C. G.; Faria, J. L. Photochemical and photocatalytic degradation of an azo dye in aqueous solution by UV irradiation. *J. Photochem. Photobiol., A* **2003**, *155* (1−3), 133−143.

(55) Soltani, T.; Entezari, M. H. Sono-synthesis of bismuth ferrite nanoparticles with high photocatalytic activity in degradation of Rhodamine B under solar light irradiation. *Chemical Engineering Journal* **2013**, *223*, 145−154.

(56) Rattan Paul, D.; Nehra, S. P. Graphitic carbon nitride: a sustainable photocatalyst for organic pollutant degradation and antibacterial applications. *Environmental Science and Pollution Research* **2021**, *28*, 3888−3896.

(57) Nadeem, M. S.; Munawar, T.; Mukhtar, F.; Ur Rahman, M. N.; Riaz, M.; Iqbal, F. Enhancement in the photocatalytic and antimicrobial properties of ZnO nanoparticles by structural variations and energy bandgap tuning through Fe and Co co-doping. *Ceram. Int.* **2021**, *47* (8), 11109−11121.

(58) Munawar, T.; Mukhtar, F.; Nadeem, M. S.; Riaz, M.; Ur Rahman, M. N.; Mahmood, K.; Hasan, M.; Arshad, M.; Hussain, F.; Hussain, A. Novel photocatalyst and antibacterial agent; direct dual Z-scheme ZnO−CeO2-Yb2O3 heterostructured nanocomposite. *Solid State Sci.* **2020**, *109*, No. 106446.

(59) Mukhtar, F.; Munawar, T.; Nadeem, M. S.; Ur Rehman, M. N.; Riaz, M.; Iqbal, F. Dual S-scheme heterojunction ZnO−V2O5−WO3 nanocomposite with enhanced photocatalytic and antimicrobial activity. *Mater. Chem. Phys.* **2021**, *263*, No. 124372.

(60) Munawar, T.; Mukhtar, F.; Yasmeen, S.; Naveed-ur-Rehman, M.; Nadeem, M. S.; Riaz, M.; Mansoor, M.; Iqbal, F. Sunlight-induced photocatalytic degradation of various dyes and bacterial inactivation using CuO−MgO−ZnO nanocomposite. *Environmental Science and Pollution Research* **2021**, *28*, 42243−42260.

(61) Ahmed, M. K.; Shalan, A. E.; Afifi, M.; El-Desoky, M. M.; Lanceros-Méndez, S. Silver-doped cadmium selenide/graphene oxide-filled cellulose acetate nanocomposites for photocatalytic degradation of malachite green toward wastewater treatment. *ACS omega* **2021**, *6* (36), 23129−23138.

(62) Liu, X.; Li, J.; Yao, W. CdS@ MoS2 hetero-structured nanocomposites are highly effective photo-catalysts for organic dye degradation. *ACS omega* **2020**, *5* (42), 27463−27469.

(63) Xu, Q.; Wageh, S.; Al-Ghamdi, A. A.; Li, X. Design principle of S-scheme heterojunction photocatalyst. *Journal of Materials Science & Technology* **2022**, *124*, 171−173.

(64) Wang, L.; Zhu, B.; Zhang, J.; Ghasemi, J. B.; Mousavi, M.; Yu, J. S-scheme heterojunction photocatalysts for CO2 reduction. *Matter* **2022**, *5* (12), 4187−4211.

(65) Xu, Q.; He, R.; Li, Y. Problems and mistakes for electron transfer mechanism in Z-scheme photocatalytic system. *Acta Phys. -Chim. Sin.* **2023**, *39* (6), No. 2211009.

(66) Eshaq, G.; ElMetwally, A. E. Bmim [OAc]-Cu2O/g-C3N4 as a multi-function catalyst for sonophotocatalytic degradation of methylene blue. *Ultrasonics sonochemistry* **2019**, *53*, 99−109.

(67) Belhouchet, N.; Hamdi, B.; Chenchouni, H.; Bessekhouad, Y. Photocatalytic degradation of tetracycline antibiotic using new calcite/titania nanocomposites. *J. Photochem. Photobiol., A* **2019**, *372*, 196−205.

(68) Qin, W.; Fang, G.; Wang, Y.; Zhou, D. Mechanistic understanding of polychlorinated biphenyls degradation by peroxymonosulfate activated with CuFe2O4 nanoparticles: Key role of superoxide radicals. *Chemical Engineering Journal* **2018**, *348*, 526−534.

(69) Yan, J.; Chen, Y.; Qian, L.; Gao, W.; Ouyang, D.; Chen, M. Heterogeneously catalyzed persulfate with a CuMgFe layered double hydroxide for the degradation of ethylbenzene. *Journal of hazardous materials* **2017**, *338*, 372−380.

(70) Nas, M. S. AgFe2O4/MWCNT nanoparticles as novel catalyst combined adsorption-sonocatalytic for the degradation of methylene blue under ultrasonic irradiation. *Journal of Environmental Chemical Engineering* **2021**, *9* (3), No. 105207.

(71) Samal, A.; Swain, S.; Satpati, B.; Das, D. P.; Mishra, B. K. 3 D Co3 (PO) 2−reduced graphene oxide flowers for photocatalytic water splitting: a type II staggered heterojunction system. *ChemSusChem* **2016**, *9* (22), 3150−3160.